Journal of Alloys and Compounds 585 (2014) 154–162

Contents lists available at ScienceDirect

Journal of Alloys and Compounds

journal homepage: www.elsevier.com/locate/jalcom

Europium-doped calcium titanate: Optical and structural evaluations

Tatiana Martelli Mazzo [a], Ivo Mateus Pinatti [a], Leilane Roberta Macario [b], Waldir Avansi Junior [c], Mario Lucio Moreira [d], Ieda Lucia Viana Rosa [a,*], Valmor Roberto Mastelaro [e], José Arana Varela [b], Elson Longo [b]

[a] INCTMN, LIEC, Departamento de Química, Universidade Federal de São Carlos, P.O. Box 676, 13565-905 São Carlos, SP, Brazil
[b] INCTMN, LIEC, Instituto de Química, Universidade Estadual Paulista, P.O. Box 355, 14800-900 Araraquara, SP, Brazil
[c] Centro de Ciências Exatas e de Tecnologia, Departamento de Física, Universidade Federal de São Carlos, Jardim Guanabara, 13565-905 São Carlos, SP, Brazil
[d] Instituto de Física e Matemática, Universidade Federal de Pelotas, P.O. Box 354, Campus do Capão do Leão, 96001-970 Pelotas, RS, Brazil
[e] Instituto de Física de São Carlos, Departamento de Física e Ciência dos Materiais, Universidade de São Paulo, P.O. Box 369, Av Trabalhador São Carlense 400, 13560-970 São Carlos, SP, Brazil

ARTICLE INFO

Article history:
Received 28 February 2013
Received in revised form 1 August 2013
Accepted 27 August 2013
Available online 21 September 2013

ABSTRACT

Pure Calcium Titanate (CT-pure) and Europium doped Calcium Titanate $Ca_{1-x}Eu_xTiO_3$ (x = 0.5%, 1.0% and 2.0% molar ratio of Eu^{3+} ions) powders were synthesized by hydrothermal microwave method (HTMW) at 140 °C for 8 min. The HTMW method appears to be an efficient method to prepare the luminescence materials using low temperatures and very short reactional times. In addition it is possible to determine specific correlations imposed by $TiCl_4$ replacement by titanium isopropoxide $[Ti(OC_3H_7)_4]$ changing the reaction character and resulting in two different options of europium doping CT syntesis. To evaluate the influence of the structural order–disorder among the reactions and different properties of these materials, the following techniques were used for characterization. XANES spectroscopy that revealed that the introduction of Eu^{3+} ions into the CT lattice induces to significant changes in the local order–disorder around both, $[TiO_6]$ and $[CaO_{12}]$, complex clusters. PL spectra show Eu^{3+} emission lines ascribed to the Eu^{3+} transitions from $^5D_0$ excited states to ^7F_J (J = 0, 1–4) fundamental states in CT:Eu^{3+} powders excited at 350 and 394 nm.

1. Introduction

Great attention has been paid recently to the development of advanced displays for multimedia applications, which can replace some cathode-ray tubes (CRTs). Field emission display (FED) is one of the best candidates for advanced flat-panel applications. Therefore, the development of phosphors suitable for FED is essential as well as the development of advanced displays likes field emission phosphors (FEDs) for multimedia application. FED phosphors are in general used to replace some Cathode Ray tubes (CRTs) because they present characteristic properties when compared to CRT phosphors, where higher voltage and higher current density are required. Therefore, research is needed for the development of new and appropriate phosphors for FEDs [1,2]. Eu^{3+} ions are significantly important due to their potential application as red phosphors, electroluminescent devices, optical amplifiers and lasers when used as doping in a great variety of materials [3–5]. The spectroscopic properties of rare earth materials have been widely studied on the basis of the crystal field splitting of the $^{2S+1}L_J$ manifolds of the $4f^6$ configuration of an Eu^{3+} ion [4–7]. The luminescence of Eu^{3+} results from the intraconfigurational f–f transitions [8] which occurs from the ^5D_J (J = 0, 1–3) and $^5L_6$ excited states to the $^7F_{J'}$ (J' = 0, 1–6) ground states. Luminescence of rare earth element doping perovskite electronic ceramics has become attractive during the past decade, not only in the use of these ions as a probe to investigate local centers and energy migration processes in the microstructures of electronic materials [9–15] but also a new technological display [16–18]. Thus, the materials activated by rare earth ions, including Sm^{3+}, Tm^{3+}, Eu^{3+}, Pr^{3+}, Tb^{3+} and Dy^{3+}, etc. are candidates in applications for advanced displays [14,19–22]. Recently, we reported photoluminescent CT:Eu^{3+} powders obtained under favorable conditions by the HTMW method at 140 °C for 10 min using $TiCl_4$ as a titanium precursor [21]. The HTMW method [21,23–25] is a genuine low temperature procedure [26] that allows high heating rates [27] and short annealing times, due to the interaction of microwave radiation with the materials. In this work, CT:Eu^{3+} phosphors were successfully prepared by the HTMW method, using titanium (IV) isopropoxide $[Ti(OC_3H_7)_4]$ as a titanium precursor at 140 °C for 8 min. $TiCl_4$ was replaced since it is an expensive reagent, highly reactive, dangerous and difficult to handle despite excellent results attained by using it to prepare $CaTiO_3$ [26,27]. Different concentrations of Eu^{3+} in the $CaTiO_3$ (CT) matrix were employed to determine the

* Corresponding author. Tel.: +55 16 3351 9308.
E-mail address: ilvrosa@ufscar.br (I.L.V. Rosa).

0925-8388/$ - see front matter © 2013 Elsevier B.V. All rights reserved.
http://dx.doi.org/10.1016/j.jallcom.2013.08.174

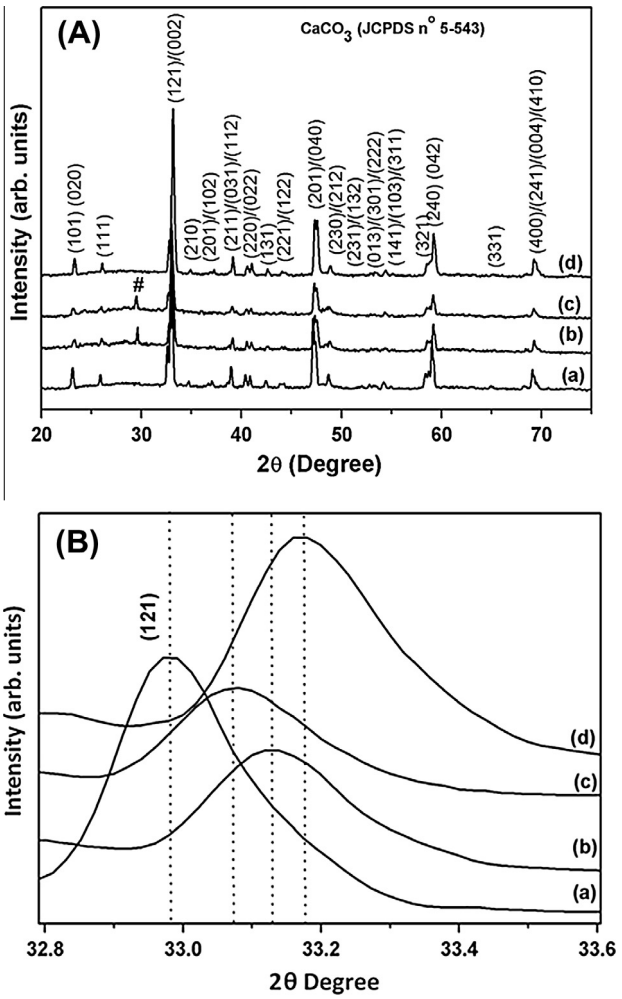

Fig. 1. (A) XRD patterns of CT-pure and CT:Eu^{3+} powders synthesized at 140 °C for 8 min. (B) Zoom of the (1 2 1) diffraction peak for samples (a) CT-pure, (b) CT:Eu^{3+} (0.5%), (c) CT:Eu^{3+} (1.0%), and (d) CT:Eu^{3+} (2.0%).

minimum concentration of this ion required to promote changes in its optical properties. To evaluate the performance of photoluminescence at room temperature, two different wavelengths of excitation energy set at 350 and 394 nm were applied. XRD, FT-Raman, ultra-violet visible (UV–vis), XAFS spectroscopy, photoluminescence and excitation emission spectra, as well as Eu^{3+} ion lifetime were employed as tools to investigate the degree of structural order–disorder of the crystalline CT:Eu^{3+} samples and the possible correlation between structural, morphological, and PL properties.

2. Experimental section

$Ca_{1-x}Eu_xTiO_3$ (x = 0.5%, 1.0% and 2.0% molar ratio of Eu^{3+} ions) powders were synthesized using [$Ti(OC_3H_7)_4$] (99.99%, Aldrich), $CaCl_2{\cdot}2H_2O$ (99.9%, Merck), Eu_2O_3 (99.999% Aldrich) and KOH (99%, Merck) resulting in CT:Eu^{3+} (0.5%) CT:Eu^{3+} (1.0%) and CT:Eu^{3+} (2.0%) powders. The solutions were prepared as follows: Firstly, 0.01 mol of the [$Ti(OC_3H_7)_4$] was slowly added to 25 mL of deionized water at 0 °C under stirring. Similarly, $CaCl_2{\cdot}2H_2O$ was dissolved in 25 mL of deionized water, separately, with stirring. To this reaction mixture were stoichiometrically added 0.5%, 1.0% and 2.0% molar of the $EuCl_3.6H_2O$ (prepared though the dissolution of Eu_2O_3 in concentrated HCl). The solution was then mixed (with constant stirring) with 50 ml of a 6.0 M KOH solution which acted as a mineralizer. This mixture was then transferred to a Teflon autoclave which was finally sealed and placed into the HTMW system using 2.45 GHz microwave radiation with a maximum power of 800 W. The reactional mixture was heated at 140 °C at nominal heating rate of 140 °C/min by direct interaction of water molecules with microwave radiation, remaining under a constant pressure of 2.5 Bar for 8 min. Then the autoclave was ambiently cooled to room temperature. Thus, the solid products were water washed several times to obtain neutral pH, and then the products were dried at 80 °C for 12 h.

CT-pure and CT:Eu^{3+} powders were characterized by XRD in a Rigaku Dmax 2500PC diffractometer using Cu Kα (λ = 1.5406 Å) radiation. XRD Data were collected from 20° to 80° in a 2θ range with a 0.5° divergence slit and a 0.3 mm receiving slit using fixed-time mode with a 0.02° step size and 1s/point. Raman spectroscopy data were obtained at room temperature using a RFS/100/S Bruker FT-Raman equipment with spectral resolution of 4 cm^{-1} attached to Nd:YAG laser, producing an excitation light of 1064 nm in the frequency range of 100 up to 800 cm^{-1}. UV–vis absorption spectra of these samples were taken using a total diffuse reflectance mode in Cary 5G equipment. PL spectra were collected with a Thermal Jarrel-Ash Monospec 27 monochromator and a Hamamatsu R446 photomultiplier. The 350.7 nm exciting wavelength of a krypton ion laser (Coherent Innova) was used. PL data of the powders was recorded with excitation at 394 nm in a Jobin Yvon–Fluorolog III spectrofluorometer at room temperature using excitation 450 W xenon lamp as excitation source. Additionally, luminescence lifetime measurements were carried out using a 1934D model spectrophosphorometer coupled to the spectrofluorometer. Finally, microstructural characterization was performed by FEG-SEM using Zeiss Supra™ 35 equipment. X-ray absorption near edge structure (XANES) spectra were measured at the titanium (Ti) and calcium (Ca) *K*-edge using a D08B-XAFS2 beam line at the Brazilian Synchrotron Light Laboratory (LNLS). The Ti and Ca *K*-edge XANES spectra were collected in samples deposited on polymeric membranes, in transmission mode at room temperature with a Si (1 1 1) channel-cut monochromator. Spectra were measured from 30 eV below and 150 eV above the edge, with an energy step of 0.3 eV near the edge region.

3. Results and discussion

Fig. 1A shows XRD patterns of CT-pure and CT:Eu^{3+} powders. The polycrystalline nature of CT powders is elucidated by XRD

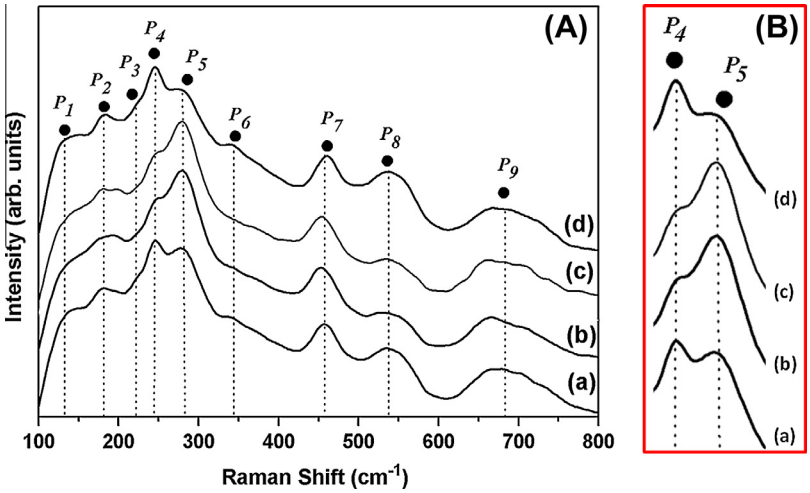

Fig. 2. (A) Raman spectra of (a) CT-pure, (b) CT:Eu^{3+} (0.5%), (c) CT:Eu^{3+} (1.0%), (d) CT:Eu^{3+} (2.0%) powders synthesized at 140 °C for 8 min. (B) Zoom of the modes ***P*****4** and ***P*****5** for the same powders.

patterns and was identified by JCPDS card (No. 22-0153) as an orthorhombic phase with *Pbnm* space group for all samples. The main diffraction peaks ascribed to (1 2 1) (0 0 2) [21,24] was used to evaluate the structural order of the material at long-range and the periodicity. The calcium carbonate ($CaCO_3$), appears in the CT:Eu^{3+} (0.5%) and CT:Eu^{3+} (1.0%) samples and were identified by JCPDS card No. 5-543.

In Fig. 1B it is possible to observe a small shifting of the corresponding peak (1 2 1) as the Eu^{3+} concentration increases and that was also observed in the previous work [20]. The inclusion of Eu^{3+} in the CT lattice results in atomic displacements and hence to a redistribution on state densities of the CT unit cell.

In the short-range, the structural behavior for CT pure Fig. 2 (a), CT:Eu^{3+} (0.5%) (b), CT:Eu^{3+} (1.0%) (c) and CT:Eu^{3+} (2.0%) (d) powders were analysed respectively by FT-Raman spectra. There are 24 Raman active modes for an orthorhombic structure with a space group *Pbnm* ($Z^B = 4$) with four molecular units in the primitive cell that can be described by representation $\Gamma_{\text{Raman-}Pbnm} = 7A_g + 5B_{1g} + 7B_{2g} + 5B_{3g}$. The nine modes observed in all samples in the range of 110–800 cm^{-1} are assigned to the orthorhombic structure, according to the literature [21,24,25,28] and can be seen in Fig. 2(A) and (B). The Raman mode located at P_1 (134 cm^{-1}) corresponds to the orthorhombic structure of the CT compound. This mode is very difficult of ascribe due to confused as a soft-mode vibration. The modes detected at $\boldsymbol{P_2}$, $\boldsymbol{P_3}$, $\boldsymbol{P_4}$, $\boldsymbol{P_5}$ and $\boldsymbol{P_6}$ (respectively at 181, 224, 244, 287 and 340 cm^{-1}) are related to vibrational modes of the bond angles O–Ti–O. The modes detected at $\boldsymbol{P_7}$ and $\boldsymbol{P_8}$ (461 and 539 cm^{-1} respectively) are related to a torsional mode in the Ti–O_6 bonds and the peak at $\boldsymbol{P_9}$ (670 cm^{-1}) is due to the symmetric stretching mode in the Ti–O bonds. A great organization in the short-range approaches was observed in all powders.

Fig. 2(B) depicts changes in the vibrational modes denoted as $\boldsymbol{P_4}$ and $\boldsymbol{P_5}$ (concerning to bond angles O–Ti–O) due to the presence of Eu^{3+}. This result indicates, possibly, that europium can also replace the Ti^{4+} (B-site) in the CT lattice. In previous published work where $TiCl_4$ was used as a Ti precursor these changes in the vibrational modes were not observed. [$Ti(OC_3H_7)_4$] presents a covalent character while $TiCl_4$ has an ionic character. In the synthesis of the CT:Eu^{3+} powders using basic conditions (KOH [6 M]), initially, occurs the hydrolysis of Ca^{2+}, Eu^{3+} and Ti^{4+} ions giving rise to the $Ca(OH)_2$, $Eu(OH)_3$ and $TiO(OH)_2$ precipitates (Eqs. (3)–(5), respectively). When $TiCl_4$ is used as a titanium precursor the lattice formation is almost instantaneous because the Ti^{4+} ions are available in the solution (Eq. (1)) due to its ionic character. On the other hand for [$Ti(OC_3H_7)_4$], the formation of the $TiO(OH)_2$ precipitates

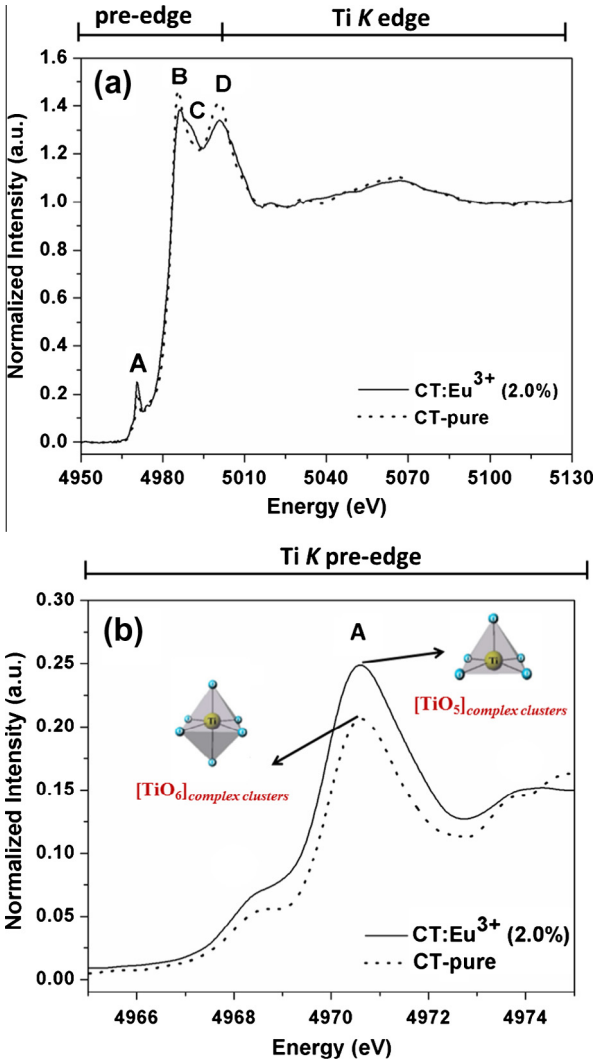

Fig. 3. (a) Ti *K*-edge XANES spectra and (b) an expanded view of the normalized XANES pre-edge region for CT-pure and CT:Eu^{3+} (2.0%) powders.

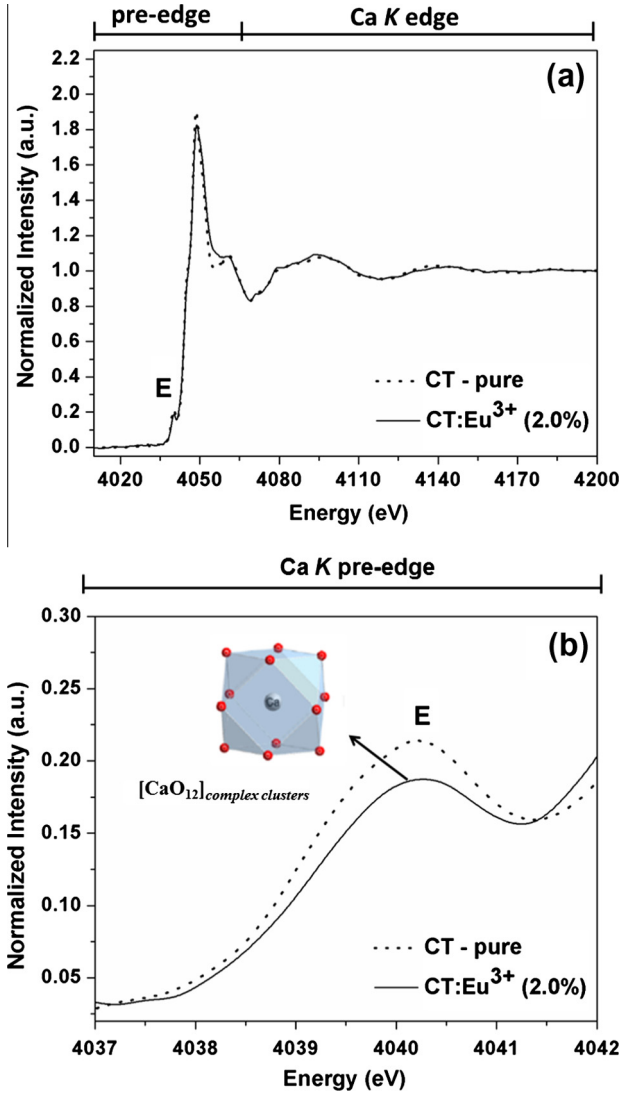

Fig. 4. (a) Ca *K*-edge XANES spectra and (b) an expanded view of the normalized XANES pre-edge region for the CT-pure and CT:Eu^{3+} (2.0%) powders.

occurs in two steps (Eqs. (2) and (3)). In this system may be occurring a competitive mechanism for the formation of the $(Ca_{1-x}Eu_x)TiO_3$ lattice between $TiO(OH)_{2(s)}$ and $Eu(OH)_3$ (Eqs. (3) and (5)).

When the bond has more covalent character the position of the Eu^{3+} ions can be present at the both sites Ca^{2+} (A-site) and Ti^{4+} (B-site), but if the bond has more ionic character the Eu^{3+} ions can be located at the Ca^{2+} (A-site) preferentially. In this case the position of Eu^{3+} in the CT lattice may be occurring at both sites A (Ca^{2+}) and B (Ti^{4+}) as observed by FT-Raman spectroscopy.

$$TiCl_{4(1)} + 4OH^-_{(aq)} \xrightarrow{KOH} Ti(OH)_{4(s)} + 4Cl^-_{(aq)} \quad (1)$$

$$[TiOCH(CH_3)_2]_{4(1)} + 2H_2O_{(1)} \xrightarrow{KOH} TiO_{2(s)} + 4(CH_3)_2CHOH_{(1)} \quad (2)$$

$$TiO_{2(s)} + 4OH^-_{(aq)} \xrightarrow{KOH} TiO((OH))_{2(s)} + H_2O_{(1)} \quad (3)$$

$$CaCl_2 \cdot 2H_2O_{(s)} + H_2O_{(1)} \xrightarrow{KOH} Ca(OH)_{2(s)} + 2Cl^-_{(aq)} + 3H_2O \quad (4)$$

$$Eu^{3+}_{(aq)} + 3OH^-_{(aq)} \xrightarrow{KOH} Eu(OH)_{3(s)} \quad (5)$$

The substitution in both A (Ca^{2+}) and B (Ti^{4+}) sites can change the composition and symmetry of the oxides creating cations or oxygen vacancies, which have a major influence on band structures, it is the main factor in determining the electronic structure [29]. In particular, these materials can accommodate rare-earth ions in both sites, so this doping ion is not only used as a probe to investigate local centers and energy [29–32], but also to provoke changes in the optical behavior of these materials [33]. The research literature confirms that the ionic ratio is dominant in justifying the rare earth ion

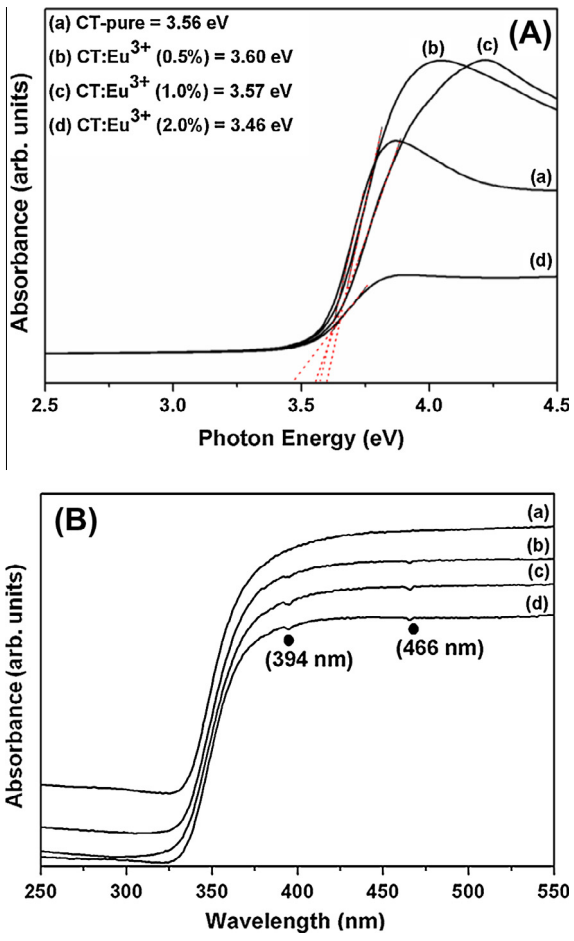

Fig. 5. (A) Diffused reflectance spectra of CT-pure and CT:Eu^{3+} powders synthesized at 140 °C for 8 min. (B) Absorption spectra of CT-pure and CT:Eu^{3+} powders. (a) CT-pure, (b) CT:Eu^{3+} (0.5%), (c) CT:Eu^{3+} (1.0%) and (d) CT:Eu^{3+} (2.0%) in both cases.

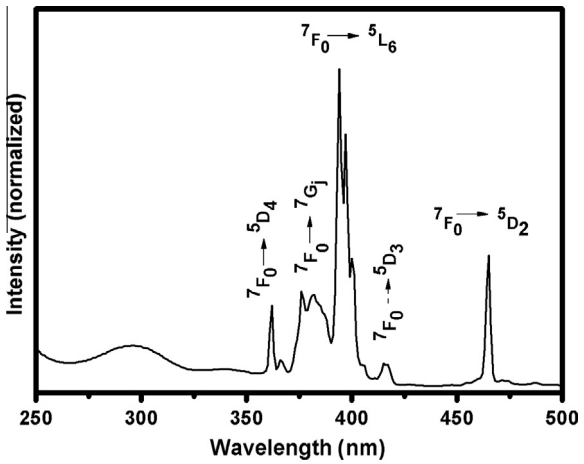

Fig. 6. Excitation spectrum of CT:Eu^{3+} (2.0%) powders synthesized at 140 °C for 8 min which were acquired by fixing the emission wavelength at 613 nm.

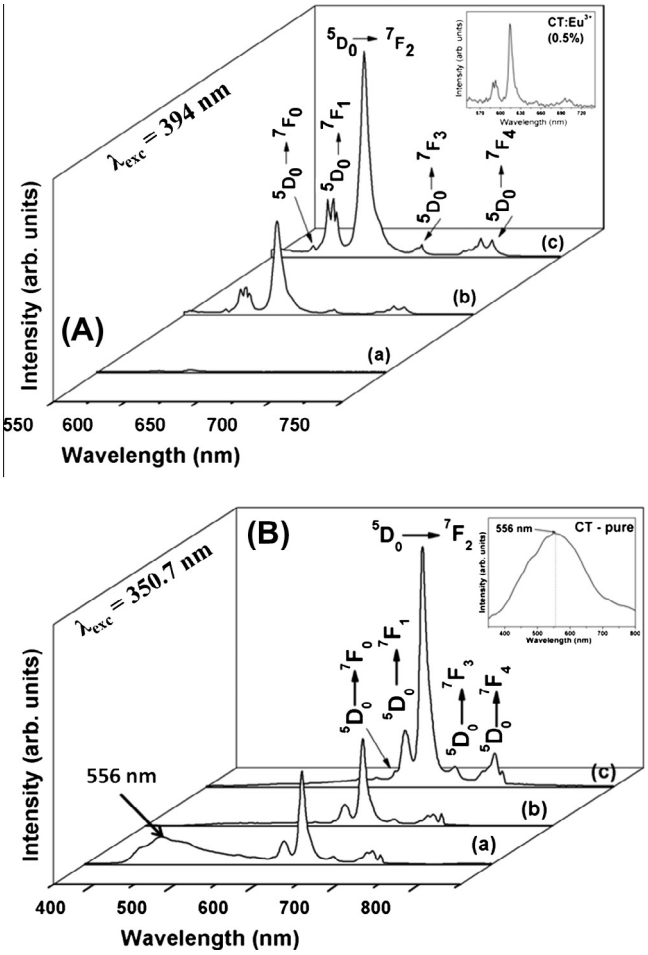

Fig. 7. PL spectra (PL) of CT:Eu^{3+} powders synthesized at 140 °C for 8 min (A) Excited at 394 nm; the insert shows the CT:Eu^{3+} (0.5%) sample at an expanded intensity scale. (B) Excited at 350.7 nm; the insert shows PL spectra of the CT-pure powder. In both spectra, (a) CT:Eu^{3+} (0.5%), (b) is the CT:Eu^{3+} (1.0%) and (c) is the CT:Eu^{3+} (2.0%) powders.

localization in perovskites and conclude that the substitution is in the A^{2+} position [34,35,36]. However, previous Rietveld refinement results of $BaTiO_3$ containing Sm^{3+} indicated that it is soluble in both the A and B sites [36]. Similarly, Araujo et al. [37] reported that the lattice location of Er^{3+} in a $SrTiO_3$ single crystal can be found in both A (Sr^{2+}) and B (Ti^{4+}) substitutional lattice sites. Using a Rietveld analysis of a nanocrystalline powder of $SrTiO_3$ containing Sm^{3+} annealed at 750 °C, Longo et al. [38] concluded that the Sm^{3+} was probably inserted in the B-site position. Zhang et al. [16] reported that Ca^{2+} and Ti^{4+} in the $CaTiO_3$ matrix can be substituted by Ln^{3+} ions.

Fig. 3(a) presents a normalized Ti *K*-edge XANES spectra of CT-pure and CT:Eu^{3+} (2.0%) powders, which reports the main important distortions around the Ca and Ti *K*-edges. XANES spectra revealed some differences in the pre- and post-edge regions. In the post-edge region it is clear that the presence of Eu^{3+} leads to a change in the peak intensities denoted as B and D, and an additional peak (denominated as C) appears in the doped powder. The pre-edge peak A also showed a higher intensity for the CT:Eu^{3+} (2.0%) powder (see Fig. 3(b)). The pre-edge feature A is attributed to the 1*s* electron transition to an unfilled *d* state. This forbidden electronic transition dipole is normally allowed by the mixture of the *p* states from the surrounding oxygen atoms into the unfilled *d* states of the titanium atoms [39].

The increase in the intensity of this peak indicates that the local environment of the Ti atom is non-centrosymmetric which, distorts the octahedral configuration [24,40,41]. In fact, the intensity of the pre-edge feature also is attributed to presence of fivefold coordinated [TiO_5] clusters [24,41]. Thus, it is clear that the presence of Eu^{3+} in this structure leads to distortion of the Ti environment. From local point of view, the analysis of the XANES at the Ti *K*-edge indicated the local polarization of [TiO_6]-[TiO_6] adjacent clusters as function of the amount of europium. The atomic volume of the Eu^{3+} ion is bigger than Ti^{4+} then it is possible that Eu^{3+}

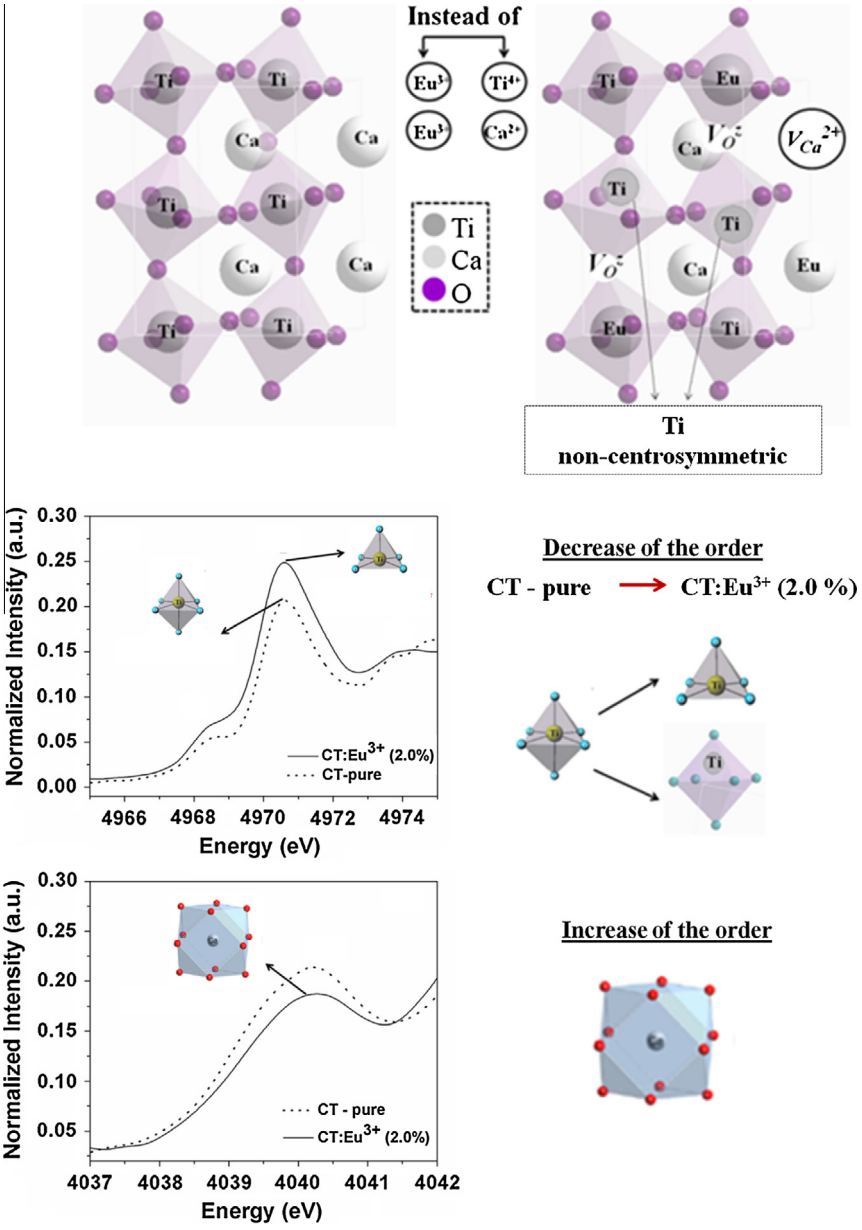

Fig. 8. Simulated orthorhombic lattice of the CT:Eu^{3+} powders synthesized at 140 °C for 8 min, presenting octahedral and dodecahedral site for Ca^{2+}, Eu^{3+} and Ti^{4+}, respectively.

replaces the B-site (Ti^{4+}) increasing the structural disorder around $[TiO_6]$ octahedral cluster related to the formation of $[EuO_6]_c^{\cdot} - [TiO_6]_c^{|}$ complex clusters [19]. Thus, the distortion between these complex clusters causes a polarization and/or difference in charge density in the structure which is able to promote a charge transfer between the $[EuO_6]_c^{\cdot} - [TiO_6]_c^{|}$ and the charge compensation occurs according to Eq. (6):

$$[EuO_6]_c^{\cdot} - [TiO_6]_c^{|} \rightarrow [EuO_6]_c^{x} + [TiO_6]_c^{x}, \quad (6)$$

where c is the complex clusters.

According to de Lazaro et al. [40], the PL emission can be related to the order–disorder in the calcium coordination which indicates that the lattice modifier affects the PL emission intensity.

To show the calcium local order, Fig. 4(a) presents the Ca *K*edge XANES spectra of CT-pure and CT:Eu^{3+} (2.0%) powders. The pre-edge feature E is commonly attributed to transitions of Ca 1*s* states to the Ca 3*d* or O 2*p* molecular orbital [24]. Peak E is attributed to the pre-edge feature which is related to the number of holes and is employed to evaluate the degree of disorder around Ca^{2+} ions [40]. As Fig. 4(b) indicates, significant changes in these features occur due to the presence of Eu^{3+}.

The decrease in the intensity of the pre-edge feature E also could be related to a increase of the order in the arrangement of nearest neighbor oxygen atoms around Ca^{2+} ions. The atomic volume of the Eu^{3+} ion is similar of the Ca^{2+} and when it replaces the A-site (Ca^{2+}) the structural order increase around the $[CaO_{12}]$ cube-octahedral cluster [19] and this fact causes the contraction in the unitary cell as observed by XRD data. In summary, the analysis of the XANES spectra collected at the Ti and Ca K-edges shows that the introduction of Eu^{3+} ions into the CT network induces significant changes in the local order–disorder around both Ti and Ca atoms.

Table 1
Relative area of the ($^5D_0 \rightarrow {}^7F_2$)/($^5D_0 \rightarrow {}^7F_1$) CT:$Eu^{3+}$ powders transition synthesized 140 °C for 8 min.

Samples	($^5D_0 \rightarrow {}^7F_2$)/($^5D_0 \rightarrow {}^7F_1$)
CT: Eu^{3+} (0.5%)	2.34
CT: Eu^{3+} (1.0%)	3.28
CT: Eu^{3+} (2.0%)	3.53

Diffuse reflectance spectra of CT–pure and CT:Eu^{3+} powders synthesized at 140 °C for 8 min are presented in Fig. 5. The existence of small absorbance peaks at 394 and 466 nm for all powders containing europium synthesized for 8 min supports the presence of Eu^{3+} in the CT lattice [21]. These peaks are also observed in excitation spectra of CT:Eu^{3+} samples (Fig. 6) and are attribute to Eu^{3+} $^7F_0 \rightarrow {}^5L_6$ and $^7F_0 \rightarrow {}^5D_2$ excitation transitions, respectively. The increase in the Eu^{3+} concentration does not provoke significant changes in the typical CT gap values estimated by the Wood and Tauc method [42]. According to this procedure these band gap values are 3.56, 3.60, 3.57 and 3.46 for of CT-pure, CT:Eu^{3+} (0.5%), CT:Eu^{3+} (1.0%) and) CT:Eu^{3+} (2.0%) powders, respectively.

Room-temperature excitation spectra (Fig. 6) of CT:Eu^{3+} powders which were acquired by fixing the emission wavelength at 613 nm, show the characteristic excitation bands of the Eu^{3+} $^7F_0 \rightarrow {}^5D_4$, ^7G_j, $^5L_6$, $^5D_3$, $^5D_2$ transition at 362, 370–391, 394, 418 and 466 nm, respectively, for all samples.

Fig. 6 shows the room temperature excitation spectrum for the CT:Eu^{3+} (2.0%) powder. A broad band is situated between 250 and 350 nm, which was attributed to charge transfer bands (CTB) between the Eu^{3+} ions and the surrounding oxygen anions [19,43–45], while the peaks between 340 and 470 nm are ascribed to f–f transitions of Eu^{3+}.

PL spectra presented in Fig. 7A and B show the Eu^{3+} emission line ascribed to transitions from the $^5D_0$ excited states to the ^7F_J (J = 0, 1–4) fundamental states of the Eu^{3+} in the CT:Eu^{3+} powders excited at 350 and 394 nm respectively. The most intense band around 613 nm is due to the $^5D_0 \rightarrow {}^7F_2$ transition. Emission spectra of all samples excited at 394 nm show $^5D_0 \rightarrow {}^7F_J$ (J = 0, 1–4) [3,21,45] Eu^{3+}transitions at 579, 589, 613, 654 and 695 nm, and of all samples excited at 350 nm (581, 594, 614, 655 and 691 nm, respectively).

In the CT:Eu^{3+} (0.5%) powder excited at 350.7 nm (Fig. 7B(a)) we observed a PL emission profile of a broadband with the maximum centred at 556 nm which is characteristic of the host matrix. CT powders synthesized using the HTMW method show that intermediate energy states within the band gap are mainly responsible for PL emission [24]. In donor perovskites like CT:Eu^{3+}, the charge compensation occurs by the formation of intrinsic defects such as Ca and/or oxygen vacancies [29]. In this case, the introduction of Eu^{3+} in the CT matrix promote distortions of the crystal lattice by the substitution of an Eu^{3+} ion in the A-site and B-sites which promote the emergence of intermediate levels within the band

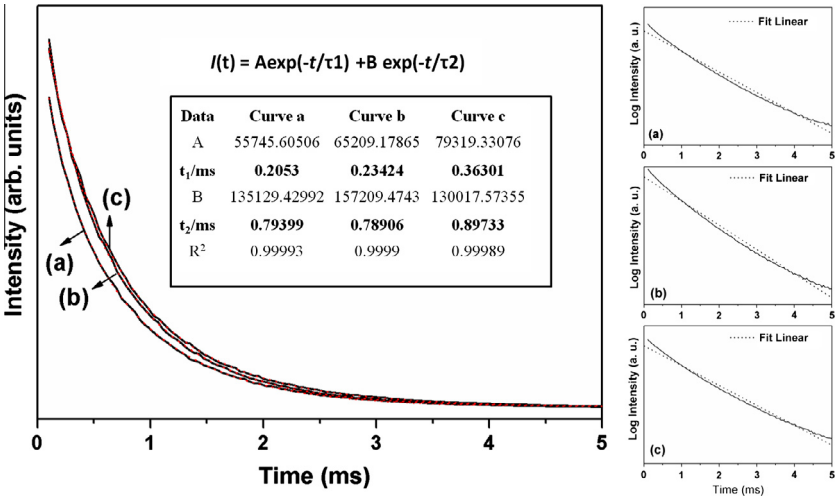

Fig. 9. Lifetime decay curves of the Eu^{3+} emission for the CT:Eu^{3+} powders synthesized at 140 °C for 8 min. Fig. (a), (b) and (c) show the linear fit at the lifetimes decay curves of the Eu^{3+} emission for the (a) CT:Eu^{3+} (0.5%), (b) CT:Eu^{3+} (1.0%) and (c) CT:Eu^{3+} (2.0%) powders, respectively.

gap, possibly due to the presence of oxygen vacancies that can be either (V_o^x), ($V_o^{\cdot}$) and ($V_o^{\cdot\cdot}$) between the clusters [BO_6] and/or Ca vacancies that can be either [$V_{Ca}^{||}$], [$V_{Ca}^{|}$] and between the clusters [AO_{12}] [21]. The optical performance of Eu-doped calcium titanates depends critically of the charge compensation according to Eqs. (7)–(10):

$$2[EuO_{12}]_c^{\cdot} + [V_{ca}^{||}O_{12}]_c \rightarrow 2[EuO_{12}]_c^{x} + [V_{ca}^{x}O_{12}]_c, \quad (7)$$

$$[TiO_6]_c^{x} + [TiO_S \cdot V_{0]_c}^{x} \rightarrow [TiO_6]_c^{|} \cdot [TiO_S \cdot V_{0]_c}^{\cdot}, \quad (8)$$

$$2[EuO_6]_c^{\cdot}[TiO_S \cdot V_{0]_c}^{x} \rightarrow 2[EuO_6]_c^{x} \cdot [TiO_S \cdot V_{0]_c}^{\cdot}, \quad (9)$$

$$[EuO_6]_c^{\cdot} + [TiO_6]_c^{|} \rightarrow [EuO_6]_c^{x} + [TiO_6]_c^{x} \quad (10)$$

where c is the complex clusters.

In Fig. 8 it is observed the simulated orthorhombic lattice of the CT:Eu^{3+} powders. The image illustrates the incorporation of Eu^{3+} in the cubo-octahedral sites (CaO_{12}) and in the octahedral sites (TiO_6).

As the Eu^{3+} concentration increases in the CT lattice, the PL emission of the host matrix is suppressed and prevailing the Eu^{3+} ion emission (see Fig. 7(B)). Therefore, that at this wavelength range, maybe, a loss of energy (non-radiative lattice vibrations) promotes the suppression of the CT host matrix PL. In this wavelength range, may be, occurs a competition between the Pl emission of the host matrix and the Eu^{3+} ion. We also observed that when powders are excited at 394 nm, only, the characteristic transitions of the Eu^{3+} ions are present; the lines are thinner and more defined possible because at 394 nm the excitation is directly of the $^5L_6$ level of the Eu^{3+} ion, as observed in the excitation spectra (Fig. 6).

The presence of a band at 581 nm is relative of the $^5D_0 \rightarrow {}^7F_0$ transition and also indicates that the Eu^{3+} ions should occupy sites

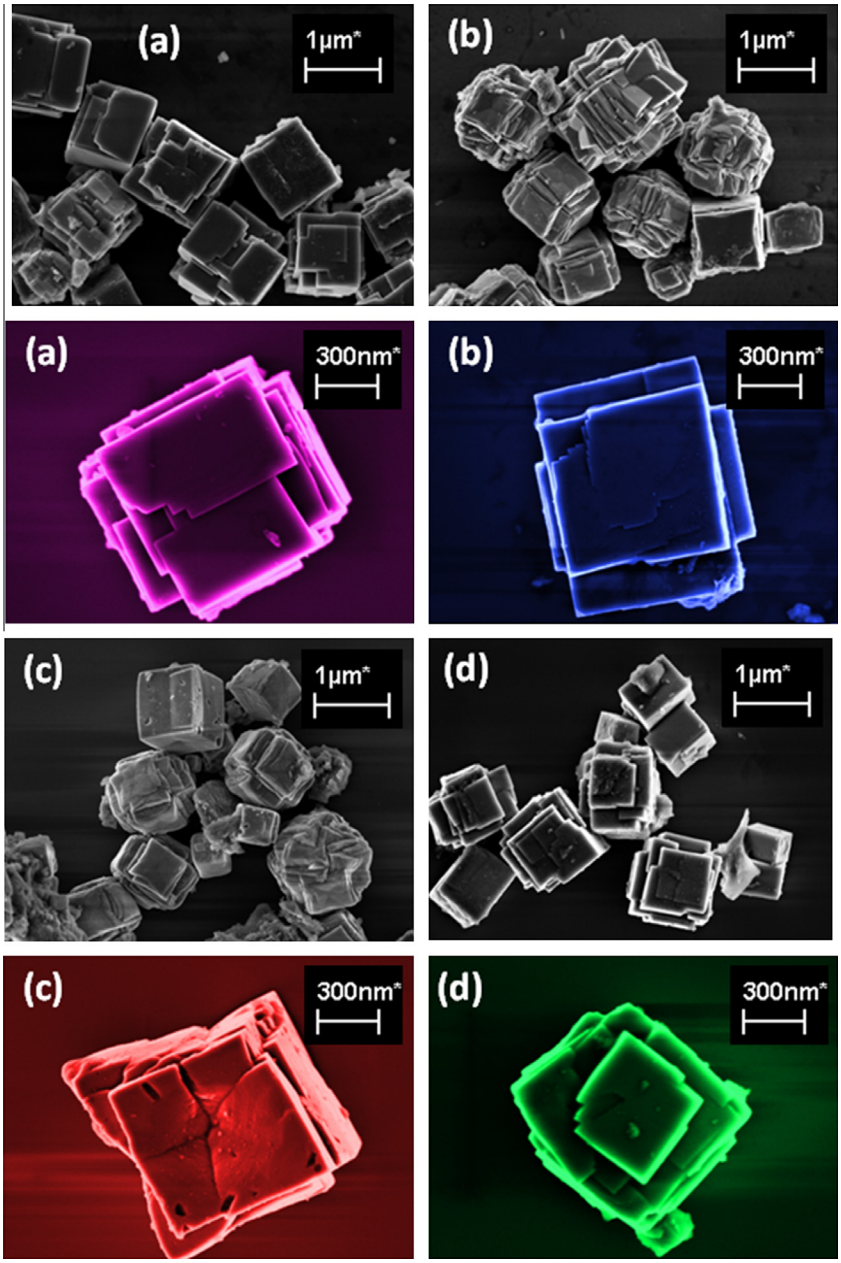

Fig. 10. FE-SEM micrograph of CT:Eu^{3+} powders synthesized at 140 °C for 8 min. Fig. (a) CT:Eu^{3+} (0.5%), (b) CT:Eu^{3+} (1.0%) and (c) CT:Eu^{3+} (2.0%) powders, respectively.

of symmetry of the type Cs, Cn or Cnv [46]. The intensity of the transition $^5D_0 \rightarrow {}^7F_2$ (hypersensitive) is strongly dependent on the Eu^{3+} environment due to its electric dipole character. However, the $^5D_0 \rightarrow {}^7F_1$ transition has a magnetic dipole character, and its intensity is almost independent of the environment. Thus, the ratio of the $(^5D_0 \rightarrow {}^7F_2)/(^5D_0 \rightarrow {}^7F_1)$ emission intensity gave us valuable information on the site symmetry in which Eu^{3+} ions are situated [20,47].

The relative area of the $(^5D_0 \rightarrow {}^7F_2)/(^5D_0 \rightarrow {}^7F_1)$, obtained from the emission spectra of the CT:Eu^{3+} powders are depicted in Table 1. By analysis of these data it is possible to surmise that the Eu^{3+} environment changes to a lower symmetry site when the europium concentration is increased since the $(^5D_0 \rightarrow {}^7F_2)/(^5D_0 \rightarrow {}^7F_1)$ relative area increases as the concentration of Eu^{3+} increases.

Fig. 9 depicts the lifetime decay curves of the $^5D_0 \rightarrow {}^7F_2$ transition for Eu^{3+} in the CT:Eu^{3+} powders using emission and excitation wavelengths fixed at 613 and 394 nm, respectively. The decay curves are well fitted by a second order exponential decay equation: $I(t) = I_1 \exp(-t/\tau_1) + I_2 \exp(-t/\tau_2)$, where I_1 and I_2 are intensities at two different interval times and corresponding decay times are τ_1 and τ_2 [48,49]. The profile of the curves clearly indicate that two processes govern the luminescence and this is a sign that the Eu^{3+} ions occupy at least two different sites of symmetry in the CT matrix (see Fig. 9(a–c)). This result supports the results FT-Raman and XANES spectroscopies data. The two lifetime and the percentage of light for each decay component are of the order $\tau_1 = 0.20$ ms (9.6%) and $\tau_2 = 0.79$ ms (90.4%) for the CT:Eu^{3+} (0.5%) powder, $\tau_1 = 0.23$ ms (11.0%) and $\tau_2 = 0.78$ ms (89.0%) for the CT:Eu^{3+} (1.0%) powder and $\tau_1 = 0.36$ ms (19.8%) and $\tau_2 = 0.89$ ms (80.2%) for the CT:Eu^{3+} (2.0%) powder, respectively. It is possible to observe a monotonic increase of the fast component when the Eu^{3+} concentration is increased.

Fig. 10 reports FE-SEM images of the CT-pure and CT:Eu^{3+} powders. In this figures it was observed micro-cube-like patterns in agreement with that the literature [21,24,50]. In Fig. 10(a–d), represent, respectively, the powders CT-pure, CT:Eu^{3+} (0.5%), CT:Eu^{3+} (1.0%) and CT:Eu^{3+} (2.0%). These micro-cube-like microcrystals are regular, with dimensions around 3.3 and 3.7 μm, very faceted and present a smooth surface that may be associated to the microwave irradiation exposure. The mechanism of the formation of the CT micro-cube occurs by the self-assembly of nano plates. This mechanism occurs by the interaction between pre-defined smaller individuals of the same origin (nano plates) and result in a specific form which is highly ordered and ends spontaneously. It is also observed that the introduction of Eu ions does not change the CT morphology.

4. Conclusions

Perovskite-type materials were obtained efficiently and quickly using low temperatures, very short reaction times and a low concentration of the rare earth ions. The PL spectroscopy of a rare earth impurity was applied as a probe to obtain structural and optical information on the CT:Eu^{3+} powders synthesized by the HTMW method. The analysis of the XANES spectra collected at the Ti and Ca *K*-edges shows that the introduction of Eu^{3+} ions into the CT network induces significant changes in the local order–disorder around both Ti and Ca atoms. Also it was possible to introduce the new less expensive and easier to handle titanium precursor to synthesize this compound. The introduction of titanium isopropoxide is the key factor to possibility the Eu doping into both Ca and Ti sites. The profile of the lifetime decay curves reveals, possibly, the presence of two sites of symmetry which are occupied by the Eu^{3+} ion in the CT matrix. Furthermore, Europium-doped calcium titanate exhibit the strongest luminescent intensity and pure red color which show that this phosphors may be more possible to be regarded as a promising candidate for applications in displays.

Acknowledgements

The authors appreciate the support of the Brazilian research financing institutions: CAPES, FAPESP/CEPID 98/14324-0, INCTMN/CNPq and FAPESP. They also wish to tanks to Rorivaldo Camargo and Madalena Tursi for technical contributions. As well as a special tanks to Prof. Osvaldo A. Serra (FFCLRP-USP) and Prof. Máximo Siu Li (IFSC-USP) for scientific contributions.

References

[1] S. Okamoto, H. Yamamoto, Appl. Phys. Lett. 78 (2001) 655.
[2] J.C. Park, H.K. Moon, D.K. Kim, S.C. Kim, K.S. Suh, Appl. Phys. Lett. 77 (2000) 2162.
[3] I.L.V. Rosa, A.P.A. Marques, M.T.S. Tanaka, D.M.A. Melo, E.R. Leite, E. Longo, J.A. Varela, J. Fluoresc. 18 (2008) 239.
[4] G. Blasse, B.C. Grabmaier, Luminescent Materials, Springer, Berlin, 1994.
[5] L. Jinsheng, Q. Bao, W. He-Rui, L. Yong, H. Ruijin, Y. Hangying, J. Mater. Sci. 46 (2011) 1184.
[6] G. Blasse, A. Bril, Philips. Tech. Ver. 31 (1970) 303.
[7] W.T. Carnall, G.L. Goodman, K. Rajank, R.S. Rana, J. Chem. Phys. 90 (1989) 3443.
[8] S.J. Korf, H.J.A. Koopmans, B.C. Lippens, A.J. Burggraaf, P.J.J. Gellings, Chem. Soc. Faraday Trans. 83 (1987) 1485.
[9] N.J. Cockroft, S.H. Lee, J.C. Wright, Phys. Ver. B 45 (1992) 9642.
[10] S. Murakami, M. Herren, S.D. Rau, M. Morita, Inorg. Chim. Acta. 300 (2000) 1014.
[11] C.T. Lin, H.Y. Lee, H.C. Bitting Jr, R.A. Lipeles, M.B. Tueling, M.S. Leung, Chem. Phys. Lett. 174 (1990) 269.
[12] H. Yugami, Y. Chiba, M. Ishigame, Solid State Ionics 77 (1995) 201.
[13] K. Toda, Y. Kameo, M. Ohta, M. Sato, J. Alloys Comp. 218 (1995) 228.
[14] W.Y. Jia, W.L. Xu, I. Rivera, A. Perez, F. Fernandez, Solid State Commun. 126 (2003) 153.
[15] M.J. Weber, R.F. Schaufele, Phys. Rev. 138 (1965) 1544.
[16] X. Zhang, J. Zhang, X. Zhang, L. Chen, Y. Luo, X. Wang, Chem. Phys. Lett. 434 (2007) 237.
[17] H. Zhang, X. Fub, S. Niu, Q. Xin, J. Alloys Comp. 459 (2008) 103.
[18] Y.C. Kang, D.J. Seo, S.B. Park, H.D. Park, Mater. Res. Bull. 37 (2002) 263.
[19] Z. Lu, L. Chen, Y. Tang, Y. Li, J. Alloys Comp. 387 (2005) L1.
[20] N.J. Cockroft, S.H. Lee, J.C. Wright, Phys. Ver. B 44 (1991) 4117.
[21] T.M. Mazzo, M.L. Moreira, I.M. Pinatti, F.C. Picon, E.R. Leite, I.L.V. Rosa, J.A. Varela, L.A. Perazolli, E. Longo, Opt. Mater. 32 (2010) 990–997.
[22] G. Daojiang, L. Yue, L. Xin, W. Yanyan, B. Jian, L. Yang, L. Mengjiao, Mater. Chem. Phys. 126 (2011) 391.
[23] S. Komarneni, R. Roy, Q.H. Li, Mater. Res. Bull. 27 (1992) 1393.
[24] M.L. Moreira, E. Paris, G. do Nascimento, V.M. Longo, J. Sambrano, V.R. Mastelaro, M. Bernardi, J. Andrés, J.A. Varela, E. Longo, Acta Mater. 57 (2009) 5174.
[25] L.S. Cavalcante, V.S. Marques, J.C. Sczancoski, M.T. Escote, M.R. Joya, J.A. Varela, M.R.M.C. Santos, P.S. Pizani, E. Longo, Chem. Eng. J. 143 (2008) 299.
[26] W. Sun, C. Li, J. Li, W. Liu, Mater. Chem. Phys. 97 (2006) 481.
[27] B.L. Newalkar, S. Komarneni, H. Katsuki, Mater. Res. Bull. 36 (2001) 2347.
[28] S. Komarneni, R.K. Rajha, H. Katsuki, Mater. Chem. Phys. 61 (1999) 50.
[29] J. Yin, Z.G. Zou, J.H. Ye, J. Phys. Chem. B 108 (2004) 8888.
[30] T.D. Dunbar, W.L. Warren, B.A. Tuttle, C.A. Randall, Y. Tsur, J. Phys. Chem. B 108 (2004) 908.
[31] A.T. de Figueiredo, S. de Lazaro, E. Longo, E.C. Paris, J.A. Varela, M.R. Joya, P.S. Pizani, Chem. Mater. 18 (2006) 2904.
[32] H. Yamamoto, S. Okamoto, H. Kobayashi, J. Lumin. 100 (2002) 325.
[33] B.A. Block, B.W. Wessels, Appl. Phys. Lett. 65 (1994) 25.
[34] S. Okamoto, H. Yamamoto, J. Appl. Phys. 91 (2002) 5492.
[35] D. Makovec, Z. Samardzija, D. Kolar, J. Solid State Chem. 123 (1996) 30.
[36] K. Ohnuma, N. Ozaki, Y. Mizuno, T. Hagiwara, K.I. Kakimoto, H. Ohsato, Ferroelectrics 332 (2006) 7.
[37] J.P. Araujo, U. Wahl, E. Alves, J.G. Correia, T. Monteiro, J. Soares, C. Boemare, Nucl. Instrum. Methods Phys. Res. Sect. B-Beam Interact. Mater. Atoms. 191 (2002) 317.
[38] V.M. Longo, M.G.S. Costa, A.Z. Simoes, I.L.V. Rosa, C.O.P. Santos, J. Andrés, E. Longo, J.A. Varela, Phys. Chem. Chem. Phys. 12 (2010) 7566.
[39] R.V. Vedrinskii, V.L. Kraizman, A.A. Novakovich, P.V. Demekhin, S.V. Urazhdin, J. Phys. Condens. Matter 10 (1998) 9561.
[40] S. de Lazaro, J. Milanez, A.T. de Figueiredo, V.M. Longo, V.R. Mastelaro, F.S. de Vicente, A.C. Hernandes, J.A. Varela, E. Longo, Appl. Phys. Lett. 90 (2007) 111904.
[41] K. Asokan, J.C. Jan, J.W. Chiou, W.F. Pong, M.H. Tsai, Y.K. Chang, Y.Y. Chen, H.H. Hsieh, H.J. Lin, Y.W. Yang, L.J. Lai, I.N. Lin, J. Solid State Chem. 177 (2004) 2639.
[42] D.L. Wood, J. Tauc, Phys. Ver. B 5 (1972) 3144.

[43] L. Jingbao, S. Xudong, L. Xiaodong, Mater. Chem. Phys. 125 (2011) 479.
[44] Z. Pei, Q. Su, S. Li, J. Lumin. 50 (1991) 123.
[45] H.W. Zheng, X.Y. Liu, W.C. Wang, H.R. Zhang, Y.X. Wang, G.S. Yin, Y.Z. Gu, W.F. Zhang, J. Sol-Gel Sci. Technol. 58 (2011) 539.
[46] M.A. Bizeto, V.R.L. Constantino, H.F. Brito, J. Alloys Comp. 311 (2000) 159.
[47] D.P. Volanti, I.L.V. Rosa, E.C. Paris, C.A. Paskocimas, P.S. Pizani, J.A. Varela, E. Longo, Opt. Mater. 31 (2009) 995.
[48] J.C. Zhang, X. Wang, X. Yao, J. Alloys Comp. 498 (2010) 152.
[49] C. Peng, Z. Hou, C. Zhang, G. Li, H. Lian, Z. Cheng, J. Lin, Opt. Express. 18 (2010) 7543.
[50] L.H. Oliveira, A.P. de Moura, T.M. Mazzo, M.A. Ramírez, L.S. Cavalcante, S.G. Antonio, W. Avansi, V.R. Mastelaro, E. Longo, J.A. Varela, Mater. Chem. Phys. (2012). http://dx.doi.org/10.1016/j.matchemphys.2012.06.042.